



CO₂-TBAB semi-clathrate hydrate dissociation behaviour in individual capsules: A new two-stage numerical model and parametric study

Yuxuan Zhang ^{a,1}, Zhongbin Zhang ^{b,1}, Xiaoqiang Zhai ^c, Yixiang Gan ^{d,e}, Benjapon Chalermsinsuwan ^f, Xiaolin Wang ^{a,*}

^a School of Engineering, The Australian National University, Canberra, ACT 2601, Australia

^b School of Energy and Mechanical Engineering, Nanjing Normal University, Nanjing, Jiangsu 210046, China

^c Institute of Refrigeration and Cryogenics, Shanghai Jiao Tong University, Shanghai 200240, China

^d School of Civil Engineering, The University of Sydney, NSW 2006, Australia

^e Sydney Nano Institute, The University of Sydney, NSW 2006, Australia

^f Department of Chemical Technology, Faculty of Science, Chulalongkorn University, Bangkok 10330, Thailand



ARTICLE INFO

Keywords:

Semi-clathrate hydrate
Dissociation kinetics
Heat and mass transfer
Encapsulation

ABSTRACT

Gas hydrates have a wide implementation in the capture, storage, transport and utilisation of a range of gases, in which the dissociation kinetics is of great importance to gas transport and recovery efficiency. Encapsulation has been proven an effective technique to enhance gas–liquid mass transfer and thus improve gas hydrate formation kinetics. However, the dissociation behaviour of gas hydrate in individual capsules remains unknown. In this work, the dissociation kinetics of encapsulated CO₂-TBAB semi-clathrate hydrates in different shapes are experimentally investigated under various operating conditions, and, for the first time, a two-stage numerical model is developed which integrates mass transfer, heat transfer and the intrinsic gas hydrate reaction kinetics to simulate the gas hydrate dissociation process. The effects of temperature, pressure, capsule volume and capsule geometry on gas hydrate dissociation kinetics are investigated. The results reveal that the proposed model is capable of capturing two distinct experimentally-observed dissociation stages, a rapid and subsequently slow stage according to the measured dissociation rate. Surface-to-volume ratio of the capsule and the dissociation driving force are the two main factors influencing the dissociation kinetics. The ring-shaped capsule exhibits the most efficient dissociation process due to its high surface-to-volume ratio and long transition time to the slow dissociation stage. This work enhances the understanding of gas hydrate dissociation behaviour in individual capsules and guides the manipulation of dissociation for efficient hydrate-based gas transport and recovery.

1. Introduction

CO₂ hydrate is an ice-like material formed by trapping CO₂ molecules into hydrogen bonded cages of water molecules under a suitable temperature and pressure condition (i.e., the phase equilibrium condition) [1]. When the temperature–pressure condition departs from phase equilibrium, hydrate dissociates and CO₂ molecules are set free as water cages dissolve. CO₂ hydrate technology can be employed in wide fields including carbon capture [2,3], storage and transport [4], gas separation [5], thermal energy storage [6], hydrate-based desalination [7], and biomass growth stimulation [8].

Generally, gas hydrate dissociation can be triggered by thermal

stimulation, depressurization, chemical inhibitor injection and the combination of these methods [9–13]. The methods of thermal stimulation and depressurization change the temperature or pressure below the phase equilibrium condition and inhibitor injection can shift the temperature–pressure equilibrium. Depressurization is considered as the most economic scheme since it does not require for external energy consumption compared to the thermal stimulation method. This scheme has been widely used in experimental studies on gas hydrate dissociation in porous sediment [14–17]. However, the gas regeneration rate of depressurization is normally low due to slow dissociation rate [9]. Thermal stimulation is energy efficient but the major weakness of this method is heat loss [18]. Chemical inhibitor injection may be more

* Corresponding author.

E-mail address: xiaolin.wang@anu.edu.au (X. Wang).

¹ The two authors have the same contribution to this study.

effective but it may potentially pollute the environment.

Understanding CO₂ hydrate dissociation kinetics is crucial for predicting gas regeneration from the view of energy recovery and remediating plugging of pipelines from the view of hydrate transportation [4]. Rapid dissociation of hydrate is desired for efficient gas regeneration and on the other hand, slow dissociation is desired during gas hydrate transport to increase transport efficiency and safety. Over the past few decades, various kinetic models have been proposed to investigate gas hydrate dissociation behaviours. The main dissociation mechanisms considered in the models include intrinsic dissociation kinetics, flow behaviours of gas and water flow, and heat and mass transfer [19]. Kim et al. [20] studied methane hydrate dissociation kinetics using a semi-batch stirred tank reactor and developed an intrinsic kinetic model. In their model, fugacity difference of methane between hydrate equilibrium condition and the decomposition condition was considered as the driving force of dissociation, and hydrate dissociation kinetics was found to be dependent on temperature, pressure and surface area of hydrate particles. It was assumed that dissociation rate is proportional to the rate constant, which can be fitted with an Arrhenius-type equation. This model was widely incorporated in kinetic models developed later to simulate gas hydrate dissociation behaviours [21–25]. Clarke and Bishnoi [26] adopted Kim's model to determine the dissociation rate constant for CO₂ hydrate at pressures ranging from 1.4 to 3.3 MPa and temperatures ranging from 274 to 281 K. The intrinsic rate constant and was found to be $1.83 \times 10^8 \text{ mol m}^{-2} \text{ Pa}^{-1} \text{ s}^{-1}$ with an activation energy of 102.88 kJ mol⁻¹. The intrinsic kinetic model was also employed to investigate dissociation characteristics in gas hydrate reservoir [27,28] and porous media [10,29,30].

Gas hydrate dissociation process is a combination of heat and mass transfer, intrinsic reaction and multiphase flow, which is suitable to investigate using computational fluid dynamics (CFD) methods. In recent years, numerous researches have been conducted on hydrate dissociation characteristics through CFD modelling. Sean et al. [31] carried out experiments and numerical simulation to study dissociation behaviour of methane hydrate ball under water flow. The driving force was defined as the Gibbs free energy difference of methane between the three-phase equilibrium condition and actual condition. The dissociation rate constant was found to be independent of pressure and can be fitted with an Arrhenius-type equation. The proposed model was proved to be applicable to describe hydrate dissociation induced by various methods including depressurization, thermal stimulation and the combination of them [32]. The model was also applied to estimate the dissociation rate of CO₂ hydrate in lab scale sediment samples [33,34]. Song et al. [35] proposed a pore scale model to simulate methane hydrate dissociation by coupling enthalpy-porosity technique with a volume of fraction (VOF) method. The model performed well in simulating the effects of phase change on heat and mass transfer, multiphase flow and pore structure evolution. Ruan et al. [36] developed a 2D axisymmetric numerical model to simulate the gas regeneration behaviour of hydrate dissociation induced by depressurization in hydrate-bearing porous medium. Various influencing factors including intrinsic porosity, initial hydrate saturation, absolute/relative permeability, etc. were studied by the numerical model. CFD methods are also widely used to investigate the effects of hydrate dissociation on hydrate slurry flow characteristics for carbon storage and transportation [23,37,38].

On the other hand, the gas–water mass transfer rate is generally restrained in both the formation and dissociation of gas hydrates in bulk liquid systems. By separating the bulk liquid phase into scattered capsules, the gas–liquid interface area can be dramatically increased. Encapsulated gas hydrate can be transported by cargo ships or carried by fluids for pipeline transport with a great potential to alleviate agglomeration and hydrate deposition in pipes. In both gas transport and recovery, hydrate dissociation behaviour is of great significance. However, although the gas hydrate formation kinetics can be greatly improved through encapsulation [39], the dissociation kinetics of encapsulated hydrates remain unknown, and to the best of authors'

knowledge, neither experiment nor simulation work has ever been done to investigate hydrate dissociation kinetics in capsules. To fill this knowledge gap, experiments were conducted under various temperature and pressure conditions to study the dissociation behaviour of gas hydrate in capsules and attempt a red blood cell (RBC) inspired encapsulation design which has been proven to greatly improve gas uptake efficiency during CO₂ hydrate formation without external energy consumption [39]. The RBC capsule is compared to a traditional spherical capsule for a comparison of gas regeneration performance. Meanwhile, a novel two-stage dissociation model is developed for the first time to simulate the hydrate dissociation process in scattered capsules with improved accuracy. The model is validated by experiment and compared to one-stage models. In addition, the effects of geometric influencing factors, including capsule volume and shape, on the capsule's gas regeneration performance are studied. The findings are expected to have wide and practical implementations in the transport and recovery of CO₂ and natural gas to improve the efficiency in the transport stage and gas recovery stage.

2. Methods

2.1. Experiments

2.1.1. Preparation of CO₂-TBAB semi-clathrate hydrate capsules

Based on the previous study [39], a spherical capsule and an RBC-shaped capsule were designed for CO₂-TBAB semi-clathrate hydrate formation experiments. TBAB was added in the solution since it can promote hydrate formation kinetics and modify the phase equilibrium conditions of CO₂ hydrate to enable the formation of hydrate within mild temperature and pressure conditions, therefore the hydrate-based carbon capture system can be operated at low cost. Although TBAB may restrain the CO₂ uptake capacity compared to pure CO₂ hydrate, by separating bulk liquid into scattered capsules, the gas–liquid contact area can be significantly increased and the disadvantages by using TBAB can be alleviated [39].

The capsules are composed of a hydrophobic breathable membrane and a mesh shell. The membrane is made of porous poly(tetrafluoroethylene) (PTFE) which can retain liquid and allow gas to penetrate. The main properties of the PTFE membrane are listed in Table 1. The shell is made of high toughness resin to stabilise the structure. Both the spherical and RBC-shaped mesh shells were produced by 3D printing. 32-wt% TBAB water solution was injected into the capsule as the semi-clathrate hydrate formation and dissociation system. The internal volume of each capsule is 22.5 mL. The schematic of the capsule structure and content is shown in Fig. 1.

The experimental apparatus mainly consists of a CO₂ gas cylinder, a thermostatic bath, a 556-mL cylindrical reactor and a data acquisition system. The schematic of the experimental apparatus is shown in Fig. 2 (a). Two thermocouples are attached to different locations in the reactor to record the temperature and a pressure transducer is used to measure the pressure. The data was logged every 10 s by the data acquisition system. Fig. 2(b) shows the internal view of the reactor with the spherical capsule.

Prior to the hydrate formation experiment, air leak test of the whole experiment system was conducted to ensure there was no gas leakage. The temperature of the thermostatic bath was set as 12 °C. The capsule was fixed inside the reactor after the temperature has stabilised. Then the residual air in the reactor was removed and CO₂ was slowly charged into the reactor until the pressure reached 4 MPa to commence the gas

Table 1

Main properties of the PTFE membrane.

Thickness (μm)	Density (kg m ⁻³)	Thermal conductivity (W m ⁻¹ K ⁻¹)	Heat capacity (J kg ⁻¹ K ⁻¹)
15	2240 – 2330	0.440 – 0.764	970 – 1090

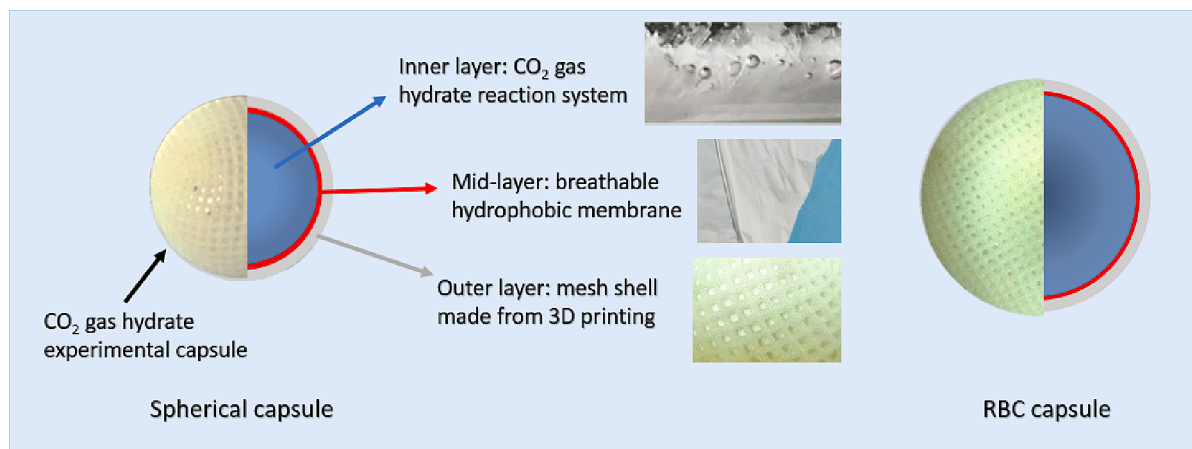


Fig. 1. Schematic of the structure of spherical and RBC-shaped capsules.

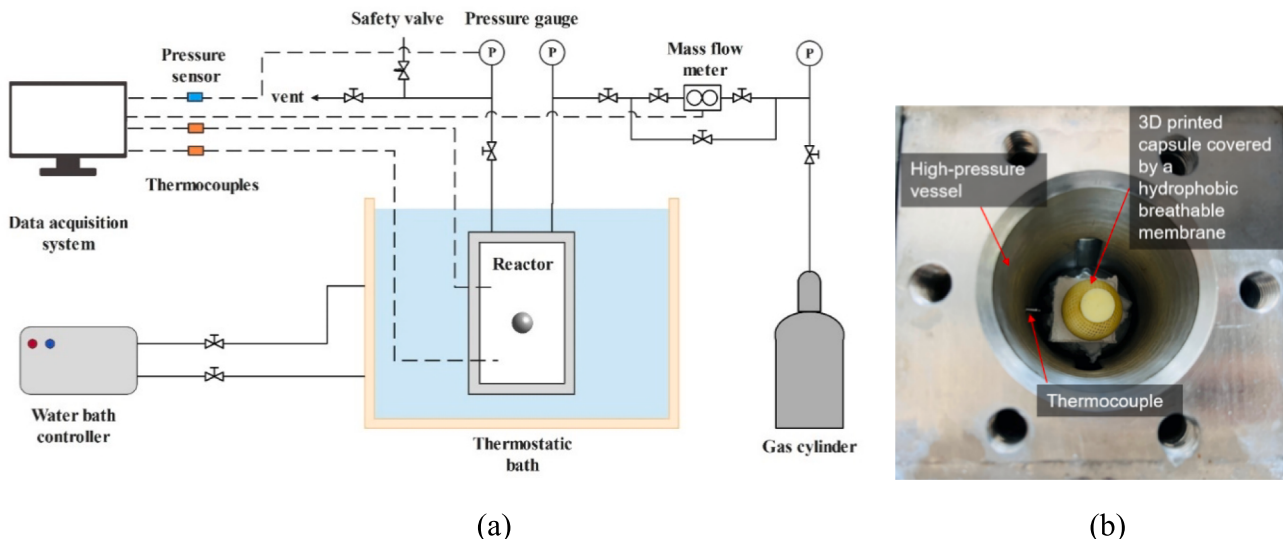


Fig. 2. Experimental setup: (a) schematic diagram of the experimental system and (b) internal view of the reactor with a spherical capsule.

hydrate formation. After 24 h, the pressure in the reactor was stable indicating the solution was converted completely into semi-clathrate hydrate. Then the capsule was used for dissociation experiments.

2.1.2. Dissociation experiments

Gas hydrate dissociation experiments were conducted under various temperature and pressure conditions above the phase equilibrium curve of CO₂-TBAB semi-clathrate hydrate. The experimental conditions are listed in Table 2. Exp. 1–4 investigates the effects of temperature under the pressure of 1 bar, and Exp. 4–7 investigates the influence of pressure under the temperature of 24 °C. Temperature is controlled by the thermostatic bath and pressure is controlled by adjusting the back pressure regulating valve. The variation of pressure in the reactor during the dissociation process was recorded for the calculation of gas regeneration. Typical experimental temperature and pressure curves over the whole dissociation process under the initial condition of 1 bar, 24 °C is shown in Fig. 3. As hydrate dissociates, the pressure in the reactor

gradually increases, and the temperature remains almost constant at 24 °C. The slight temperature drop may be caused by the endothermic effect during dissociation.

The cumulative gas regeneration can be calculated by:

$$n_{\text{CO}_2,\text{tot}} = n_{\text{CO}_2,g} + n_{\text{CO}_2,l} \quad (1)$$

where $n_{\text{CO}_2,\text{tot}}$ is the total mole of CO₂ regeneration, $n_{\text{CO}_2,g}$ is the amount of CO₂ in the gas phase produced by hydrate dissociation, and $n_{\text{CO}_2,l}$ is the amount of CO₂ dissolved in the liquid phase.

$n_{\text{CO}_2,g}$ can be calculated by:

$$n_{\text{CO}_2,g} = n_i - n_0 = \frac{P_i V_g}{Z_i R T_i} - \frac{P_0 V_g}{Z_0 R T_0} \quad (2)$$

where P is the pressure, V is the volume of gas, R is the ideal gas constant, T is the temperature, and Z is the gas compressibility factor. Subscripts i and 0 represent the actual and initial state of hydrate dissociation, respectively. The composition of hydrate is proved to be 2.49CO₂-TBAB-38H₂O in a previous study [40]. Therefore, the cumulative CO₂ regeneration can be associated with the mole number of hydrate:

$$n_{\text{CO}_2,\text{tot}} = 2.49 \times (n_{0,\text{hyd}} - n_{i,\text{hyd}}) \quad (3)$$

Table 2
Temperature and pressure conditions for dissociation experiments.

Exp. No.	1	2	3	4	5	6	7
Temperature (°C)	18	20	22	24	24	24	24
Pressure (bar)	1	1	1	1	6	11	16

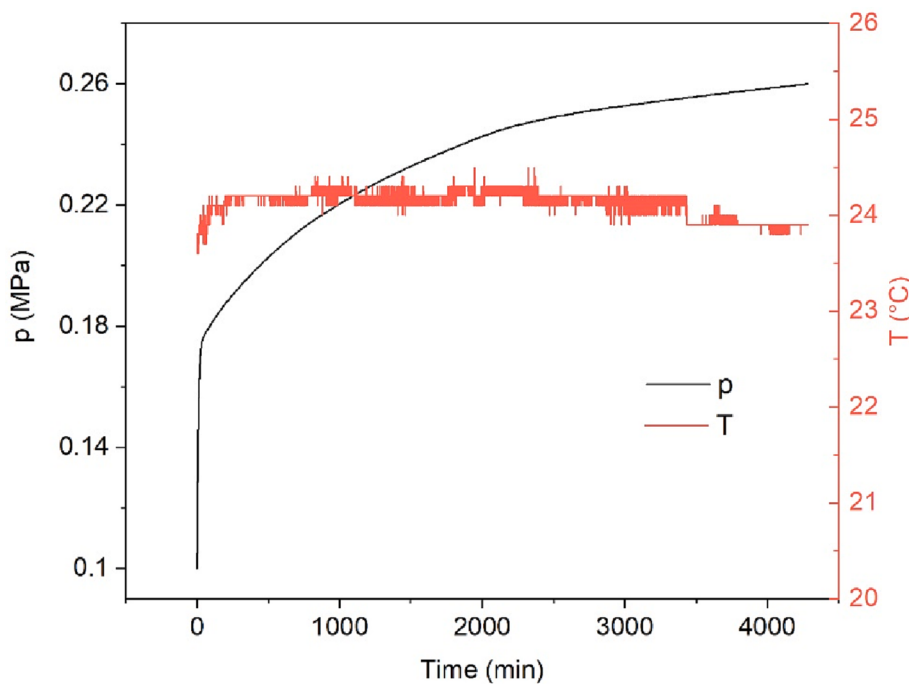


Fig. 3. Pressure and temperature variation over time under the initial condition of 1 bar, 24 °C.

2.2. Model development

Based on the findings from previous studies [31–33], the driving force of gas hydrate dissociation can be described as the difference in Gibbs free energy between the hydrate phase and ambient phase, and this theory can be applied to predict hydrate dissociation process induced by different methods including temperature increase, depressurisation or simultaneous change in pressure and temperature. This basic idea is adopted and extended in this study.

For hydrate dissociation in a spherical capsule, the overall process can be divided in two stages. In the first stage (Stage 1), hydrate capsule is exposed in gas, and the Gibbs free energy difference can be expressed in terms of the fugacity difference between the gas under three-phase equilibrium condition and actual condition. As hydrate dissociates, the hydrate gradually sinks due to density difference between hydrate and solution until it is submerged in the solution. Then hydrate dissociation process enters the second stage (Stage 2), in which the Gibbs free energy difference is expressed in terms of the concentration difference between the gas in the aqueous phase under three-phase equilibrium condition and the actual condition [31]. A schematic of hydrate dissociation in

different stages is shown in Fig. 4.

To simulate the dissociation kinetics of the gas hydrate capsule, some assumptions and simplifications are made for the numerical model:

- (1) Dissociation only occurs at the hydrate surface.
- (2) The spherical capsule shrinks uniformly inward along the radius during dissociation.
- (3) The solubility of CO₂ in the TBAB solution follows Henry's law.
- (4) The dissociation process transits from Stage 1 to Stage 2 when the hydrate is fully immersed in the solution.

Since the reactor and hydrate capsule are axisymmetric, the model can be developed in a 2D approach as shown in Fig. 5.

2.2.1. Surface dissociation kinetics

It is assumed that the surface dissociation flux (F , mol m⁻² s⁻¹) of the hydrate is proportional to the driving force, then the dissociation flux in different stages can be expressed as:

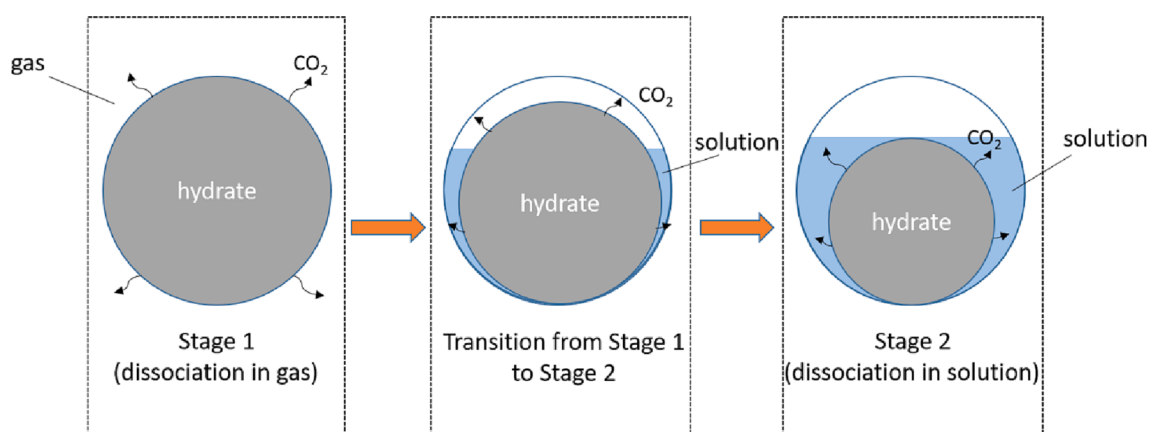


Fig. 4. Schematic of hydrate dissociation in different stages.

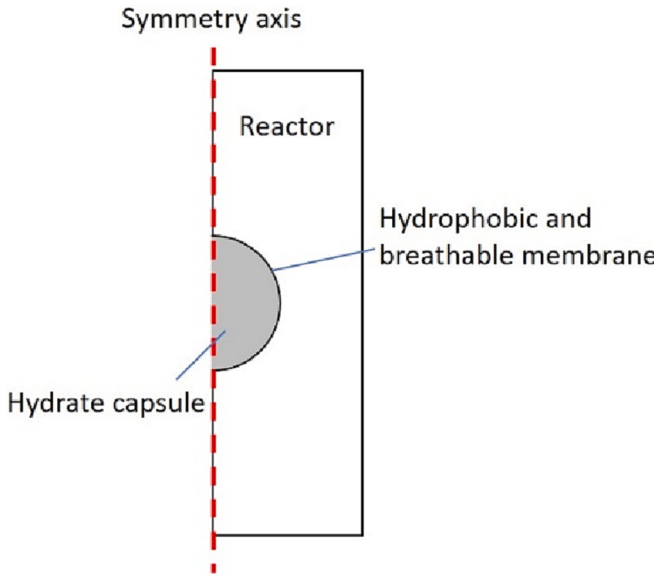


Fig. 5. Schematic of the numerical model developed in a 2D axisymmetric approach.

$$F_1 = K_1 RT \ln \frac{f_e}{f}, \text{ Stage 1}; \quad (4)$$

$$F_2 = K_2 RT \ln \frac{C_e}{C}, \text{ Stage 2}. \quad (5)$$

where K_1 and K_2 are dissociation rate constants of Stage 1 and 2, respectively. R is the ideal gas constant, T is the temperature, f_e and f are the fugacity of CO_2 equilibrated with hydrate in the gas phase and that at the hydrate surface in actual conditions, respectively. C_e and C are the concentration of CO_2 equilibrated with hydrate in the liquid phase and that at the hydrate surface in actual conditions, respectively. The three-phase equilibrium condition of $\text{CO}_2 + \text{TBAB} + \text{H}_2\text{O}$ system is predicted based on the thermodynamic model proposed by Patrice [41], the solubility of CO_2 is determined based on the data of Larryn et al. [42], and the fugacity of CO_2 is given by [43]:

$$f = p \exp\left(\frac{Bp}{RT}\right) \quad (6)$$

$$\begin{aligned} \frac{B}{\text{cm}^3 \cdot \text{mol}^{-1}} = & -1636.75 + 12.0408\left(\frac{T}{\text{K}}\right) - 3.27957 \times 10^{-2}\left(\frac{T}{\text{K}}\right)^2 + 3.16528 \\ & \times 10^{-5}\left(\frac{T}{\text{K}}\right)^3 \end{aligned} \quad (7)$$

2.2.2. Mass transfer equations

The basic mass transfer equation of CO_2 transport is:

$$\frac{\partial c_g}{\partial t} = D_g \nabla^2 c_g \quad (8)$$

where c_g is the concentration of CO_2 , and D_g is the diffusion coefficient of CO_2 . The diffusion coefficient of CO_2 is estimated based on the work of Li et al. [44].

At the surface of the hydrate, a continuity boundary condition is applied:

$$K_1 RT \ln \frac{f_e}{f} = D_g \nabla c_{gs}, \text{ Stage 1}; \quad (9)$$

$$K_2 RT \ln \frac{C_e}{C} = D_g \nabla c_{gs}, \text{ Stage 2}. \quad (10)$$

where c_{gs} is the concentration of CO_2 at the hydrate surface.

For the membrane side, the boundary conditions are:

$$-\mathbf{n} \cdot \mathbf{J}_u = \frac{D_m}{d_m} (c_{g,d} - c_{g,u}) \quad (11)$$

$$-\mathbf{n} \cdot \mathbf{J}_d = \frac{D_m}{d_m} (c_{g,u} - c_{g,d}) \quad (12)$$

where \mathbf{J} is the diffusion flux, and subscripts u, d represent the upside and downside of the membrane, respectively. D_m is the diffusion coefficient of CO_2 in the membrane, and d_m is the thickness of the membrane.

No flux boundary condition is applied at the boundaries of the reactor:

$$-\mathbf{n} \cdot \mathbf{J} = 0 \quad (13)$$

2.2.3. Heat transfer equations

Conduction is the main mode of heat transfer in the system and the governing equation is given by:

$$\rho C_p \frac{\partial T}{\partial t} - k \nabla^2 T = Q \quad (14)$$

where ρ , C_p , T , k , and Q represent the density, heat capacity, temperature, thermal conductivity and the latent heat of hydrate dissociation, respectively.

The boundary condition at the surface of hydrate is given by:

$$\dot{Q} + k_h \nabla T_h = k_i \nabla T_i \quad (15)$$

where \dot{Q} is the heat flux induced by hydrate dissociation, k_h is the thermal conductivity of hydrate and k_i is the thermal conductivity of the ambient gas/liquid phase.

For the boundaries of the air in the reactor, constant temperature condition is employed:

$$T = T_s \quad (16)$$

2.2.4. Volume change as hydrate dissociates

The hydrate capsule gradually shrinks as hydrate dissociates. For the spherical capsule, the radius of the hydrate can be associated with the total mole numbers of gas regeneration:

$$\frac{r_i^3}{r_0^3} = 1 - \frac{n_{\text{CO}_2,\text{tot}}}{n_0} \quad (17)$$

where r_i is the radius of hydrate, and r_0 is the initial radius of the hydrate capsule, $n_{\text{CO}_2,\text{tot}}$ is the cumulative gas regeneration, and n_0 is the theoretical maximum gas regeneration.

At the point when hydrate is completely immersed in solution (as shown in stage 2 in Fig. 4), the following equation can be derived:

$$V_0 - V_i - V_{\text{cap}} = \frac{V_0 - V_i}{\alpha} \quad (18)$$

where V_0 and V_i are the initial and actual volume of the hydrate respectively, V_{cap} is the volume of the gas cap, α is the shrinkage factor of hydrate during dissociation, which can be determined based on the density of hydrate and solution. It's measured that the density of TBAB solution in the experimental conditions is 1036 g cm^{-3} , and the density of hydrate is approximately 1060 g cm^{-3} [45], therefore, the volume of hydrate will shrink by a factor of 1.085 during dissociation. Combining equation (17) and (18), the cumulative gas regeneration can be calculated at the transition point of Stage 1 and Stage 2.

To find the reaction rate constants K_1 and K_2 , levenberg–marquardt algorithm [46] is employed using the least-squares objective for the simulation and experiment results. Mean relative difference (MRD) between the experiment and simulation results is calculated to quantify the accuracy of the model, which is defined by:

$$MRD = \frac{1}{N} \times \frac{\sum |x_{i,\text{sim}} - x_{i,\text{exp}}|}{x_{i,\text{exp}}} \times 100\% \quad (19)$$

where N represents the number of data points.

3. Results and discussion

3.1. Experimental results

3.1.1. CO_2 -TBAB semi-clathrate hydrate dissociation kinetics at different pressures

Fig. 6 shows the time evolutions for the gas regeneration rate of the whole CO_2 -TBAB semi-clathrate hydrate dissociation process in the spherical capsule at different initial pressures. Two distinct stages can be clearly observed for all the pressure conditions. At first, the hydrate dissociated rapidly which caused a rapid pressure increase in the reactor. Then the dissociation rate gradually decreased and the accumulated gas slowly grew until the maximum gas regeneration was reached. The variation in hydrate dissociation rate can be attributed to two reasons. Firstly, the total surface area of the hydrate decreased as it dissociated, and a smaller dissociation area (fewer dissociation sites) led to a lower gas regeneration rate. Secondly, as described in section 2.2, the surrounding conditions change during hydrate dissociation, i.e. hydrate dissociated in the gas phase before in the liquid phase, which caused different mechanisms of driving force in the two stages. Fugacity difference was the driving force in the first stage (the hydrate core dissociating in gas) while concentration difference is the driving force in the second stage (the hydrate core dissociating in solution), which is the other reason for distinguishably different gas regeneration rates in the two periods.

As expected, the time required to complete the dissociation increases with an increased initial pressure, which is due to the weaker dissociation driving force at higher pressures. In Stage 1 the fugacity of CO_2 increased with a raised pressure within the pressure range studied, while in Stage 2 the solubility of CO_2 in solution increased at higher pressures, which resulted in a higher concentration of CO_2 in the liquid—both leading to weakened dissociation driving force. The gas generation rate

from hydrate also differs at different pressures, as shown in **Fig. 6**. In the beginning, the gas generation rate decreases with increasing pressure, which, however, later on increases with the increase of pressure (as shown in the inserts of **Fig. 6**). The reason is that in the initial stage, the dissociation surface area of hydrates was the same for all cases, and the gas generation rate was higher for the cases with a stronger driving force, as in the early period the driving force is the leading factor to dissociation kinetics. At a later stage, hydrate that dissociated at a higher pressure, as the dissociation went slowly, remained a much larger surface area than that dissociated at a lower pressure, which leads to a higher gas generation rate. At the time, the surface area of hydrates becomes a dominant factor. However, as the gas regeneration rate is very low for all the cases at the later stage, its influence on the overall gas regeneration yield is marginal.

3.1.2. CO_2 -TBAB semi-clathrate hydrate dissociation kinetics at different temperatures

Fig. 7 shows the time evolutions for gas regeneration yield and gas generation rate of the spherical hydrate capsule at different temperatures. The two-stage process is also clear for the gas regeneration profile at each temperature, and the reasons are the same as those explained in the last section. A higher temperature results in a more rapid dissociation process since temperature has significant effects on the driving force of dissociation. With the increase of temperature, both the fugacity and concentration of CO_2 that is equilibrated with hydrate will correspondingly increase, which causes a larger Gibbs free energy difference between the equilibrium condition and actual condition in experiments, i.e. a larger dissociation driving force in Stage 1 and 2. As shown, the time required for 90% of hydrate dissociation (denoted as n_{90}) at 18°C is 5,010 min, while that is 1,917 min at 24°C , which is shortened by 61.7%. Therefore, the temperature has a significant influence on the hydrate dissociation kinetics. In the later stage of dissociation, the gas generation rate reduces as the temperature rises, due to the smaller hydrate surface area resulting from the earlier rapid dissociation at a higher temperature. However, the effect of dissociation surface area in this stage is insignificant on the overall gas regeneration.

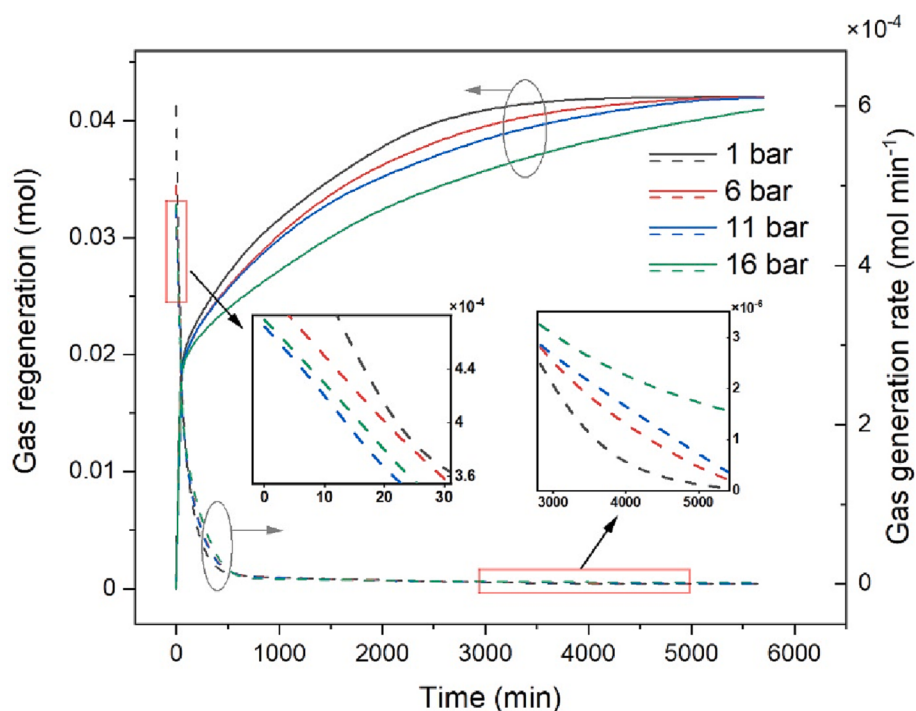


Fig. 6. Gas regeneration of hydrate in the spherical capsule at different initial pressures.

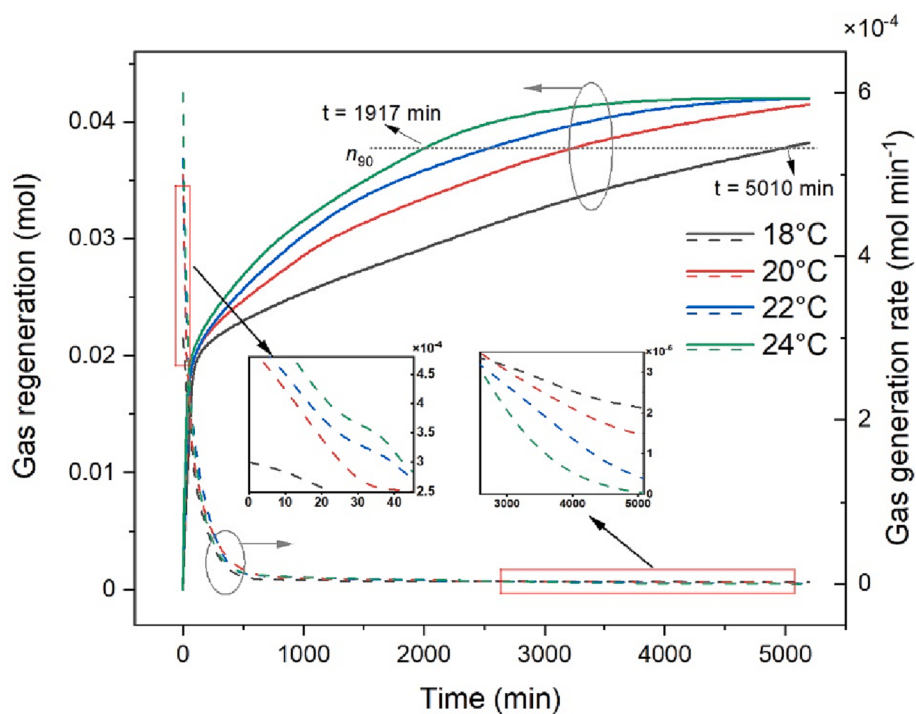


Fig. 7. Gas regeneration of hydrate in the spherical capsule at different temperatures.

3.1.3. Comparison between spherical and RBC-shaped capsules

The RBC geometry has been found effective in promoting hydrate formation kinetics. In hydrate dissociation, the gas regeneration profiles of the spherical and the RBC-shaped capsules are compared under the condition of 24 °C and 1 bar in Fig. 8. Compared to the spherical hydrate capsule, the transition from Stage 1 to Stage 2 happens earlier for the RBC-shaped capsule. According to a geometric study based on the capsule shapes and the density difference between gas hydrate (1060 g

cm^{-3}) and solution (1036 g cm^{-3}), the theoretical transition point is reached (the state of the shapes in Fig. 9) when cumulative gas regeneration is 0.013 mol for the RBC-shaped capsule and 0.020 mol for the spherical capsule, which is consistent with the experiment results. In each stage, the gas generation rate of the RBC-shaped capsule is higher than the spherical capsule, due to the larger hydrate surface area in the RBC-shaped capsule. Therefore, although the cumulative gas regeneration yield of the RBC-shaped hydrate is lower than that of the spherical

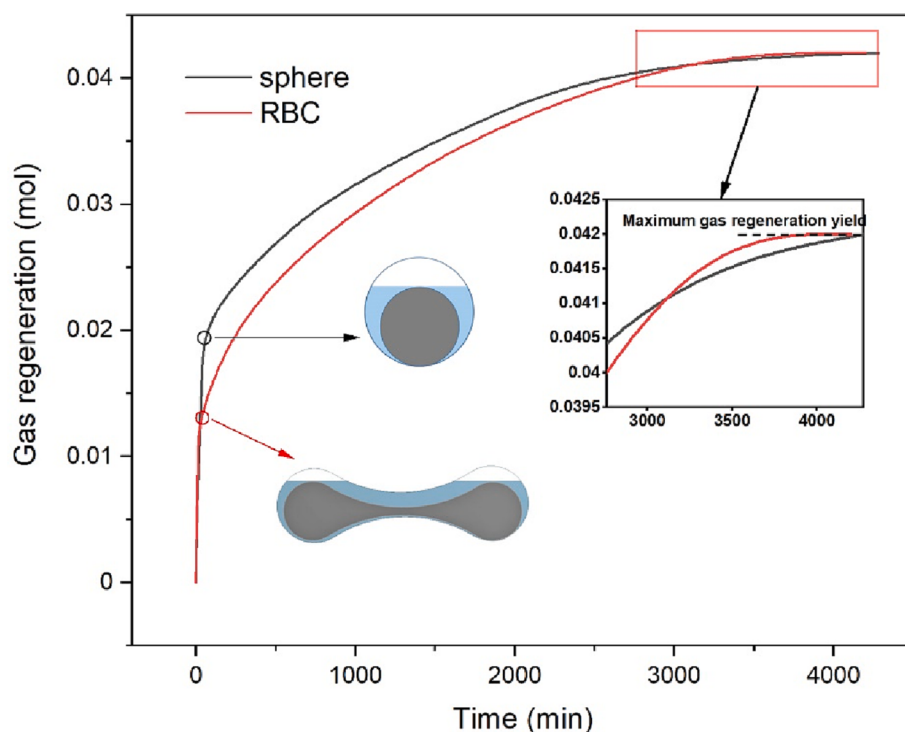


Fig. 8. Gas regeneration profiles of hydrate in the spherical and the RBC-shaped capsules at 1 bar, 24 °C.

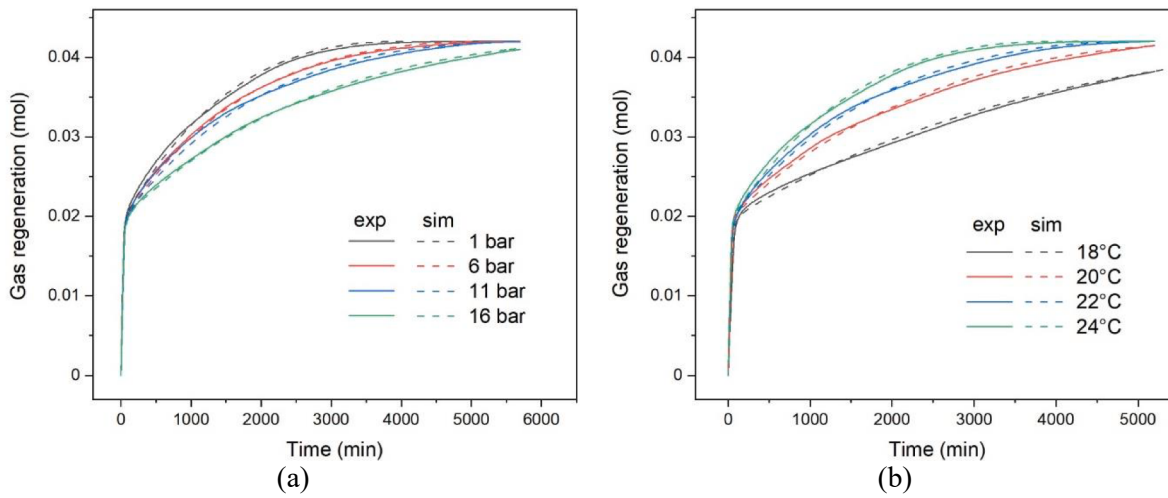


Fig. 9. Validation of gas hydrate dissociation in the spherical capsule at (a) different pressures, with temperature of 24 °C and (b) different temperatures, with pressure of 1 bar.

hydrate in the middle period of dissociation due to earlier transition to the slow dissociation stage (stage 2), the time for completing dissociation is slightly shorter than the spherical one.

The performance of RBC-shaped encapsulation in enhancing CO₂ hydrate dissociation kinetics is not as extraordinary as that in the hydrate formation process [39]. The reason is that during hydrate formation, CO₂ diffuses through the hydrate layer to react with the solution at the inner part of the capsule on the phase interface [47]. As the diffusion coefficient of CO₂ in hydrate layer is very low, diffusion distance is important and greatly influences the hydrate formation kinetics. RBC has a shorter distance from the surface to the hydrate core due to its biconcave disc shape, therefore the RBC-shaped encapsulation can significantly improve hydrate formation kinetics. However, in hydrate dissociation process, dissociation mainly happens at the surface of hydrate, so the advantage of RBC with shorter diffusion distance is not significant. According to the gas regeneration profiles of spherical and RBC-shaped hydrate, driving force is the main factor affecting the dissociation kinetics rather than the gas diffusion distance. The dissociation rate of hydrate in the gas phase is overall much higher than that in the liquid phase when hydrate is immersed in the solution. In realising this difference between the formation kinetics and the dissociation kinetics, a further geometric parametric study is conducted for hydrate dissociation as presented in section 3.2.5.

3.2. Simulation results

3.2.1. Validation of two-stage dissociation models

The simulation results of the dissociation process of the spherical capsule under various temperature and pressure conditions are compared with the experimental results in Fig. 9 (a) and (b). MRD values between the experiment and simulation results are listed in Table 3. The maximum MRD for the investigated conditions is 4.42%, therefore, by dividing the hydrate dissociation process into two stages and modelling them separately, the numerical model can well predict the dissociation process in a capsule.

3.2.2. Comparison of one-stage and two-stage dissociation models

Clarke and Bishnoi [26] modelled the dissociation kinetics of CO₂ gas hydrates using a semi-batch stirred tank reactor. In their model, fugacity difference is considered as the driving force and the hydrate dissociation rate is modelled as:

$$\frac{dn}{dt} = k_{D0} \exp\left(-\frac{\Delta E}{RT}\right) (f_{eq} - f_g) \quad (20)$$

where k_{D0} is the reaction rate constant, ΔE is the activation energy, f_{eq} and f_g is the fugacity of CO₂ in the equilibrium condition and actual condition, respectively. As agitation is used in the experiment, hydrate particles can be considered to dissociate in the gas phase, so it is not applicable in the scenario when hydrate is immersed in the solution without agitation.

Ayako et al. [34] proposed a model to simulate CO₂ hydrate dissociation under water flow conditions. Hydrate dissociation is driven by low concentration of CO₂ in the fresh water flow and the dissociation rate is expressed as:

$$\frac{dn}{dt} = k_{bl} RT \ln \frac{C_H}{C_l} \quad (21)$$

where k_{bl} is the dissociation rate coefficient, C_H is concentration of CO₂ equilibrated with hydrate in the solution, and C_l is the actual concentration of CO₂ at hydrate surface.

Using Clarke-Bishnoi model and Ayako model, the gas regeneration yield of encapsulated CO₂ gas hydrate was calculated based on the experimental conditions of the present work. Fig. 10 shows the comparison among Clarke-Bishnoi model, Ayako model, and the two-stage model proposed in this paper to simulate the dissociation process of the spherical capsule under the condition of 1 bar and 24 °C. It can be observed that two-stage model has better accuracy in predicting the dissociation process of hydrate in capsules than any one-stage models. Therefore, for encapsulated hydrate cases, a two-stage model is necessary as justified by the physical mechanisms and the comparison results of different models.

3.2.3. Determination of reaction rate constants

The effects of pressure and temperature on reaction rate constants are studied through the proposed model. Fig. 11 shows the influence of pressure on the optimised reaction rate constants K_1 and K_2 in Stage 1 and Stage 2. The reaction rate constants show weak dependence on pressure at the investigated conditions. The average value of K_1 and K_2 is 1.90×10^{-7} and $1.33 \times 10^{-8} \text{ mol}^2 \text{ m}^{-2} \text{ s}^{-1}$ respectively, and the

Table 3
Mean relative difference between the experiment and simulation results.

Case	1	2	3	4	5	6	7
Temperature (°C)	18	20	22	24	24	24	24
Pressure (bar)	1	1	1	1	6	11	16
MRD (%)	3.37	4.02	3.51	3.83	2.99	4.42	2.31

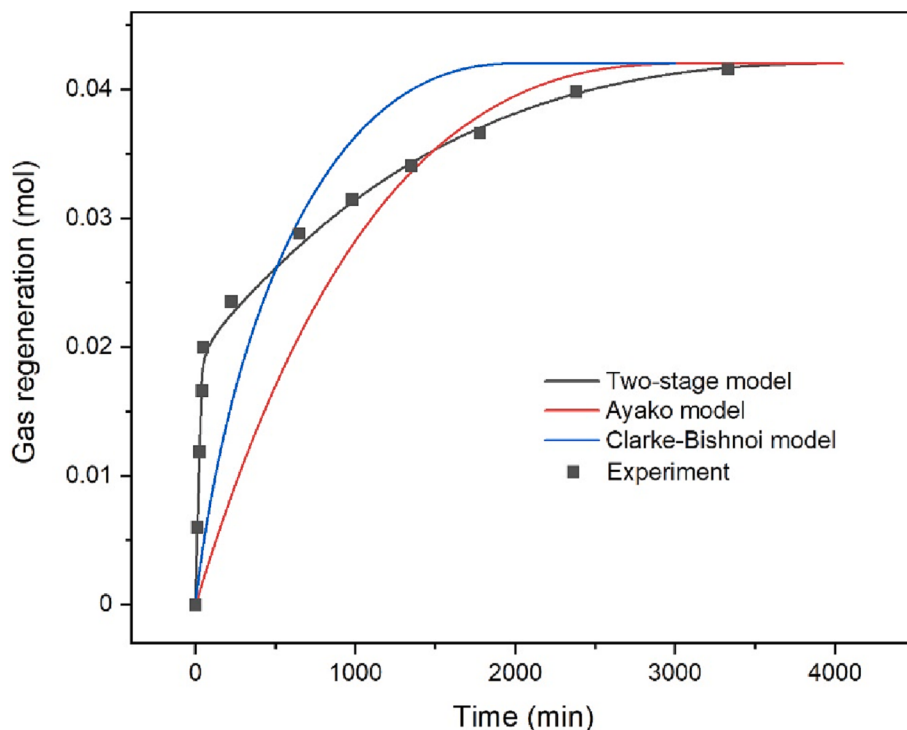


Fig. 10. Comparison between different kinetic models on simulating gas hydrate dissociation.

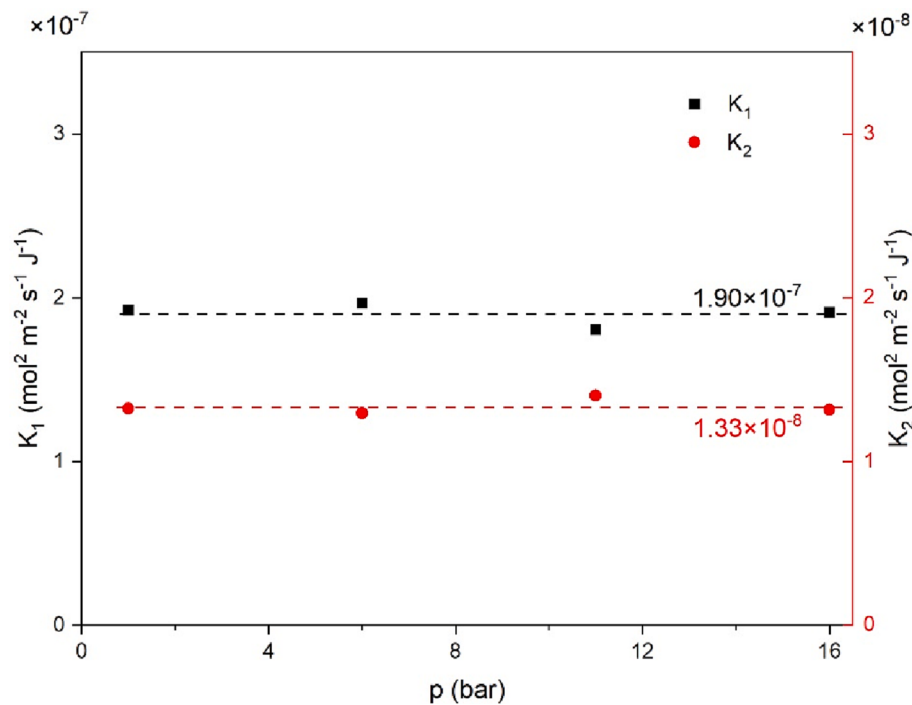


Fig. 11. Influence of pressure on K_1 and K_2

value of each data point floats around the average value. The independence of reaction rate constant on pressure was also observed in other hydrate dissociation models [20,26,31].

To investigate the influence of temperature on reaction rate constants, an Arrhenius-type equation was adopted based on the results of previous studies [26,31,33]. The reaction rate constants can be expressed as:

$$K_1 = K_{10} \exp\left(-\frac{\Delta E_1}{RT}\right) \quad (22)$$

$$K_2 = K_{20} \exp\left(-\frac{\Delta E_2}{RT}\right) \quad (23)$$

where K_{10} and K_{20} are the pre-exponential factors, ΔE_1 and ΔE_2 is the activation energy in Stage 1 and Stage 2, respectively. The relationship

of $\ln(K)$ and $1/T$ is plotted in Fig. 12 and a linear fit is conducted for both stages. Good agreement can be achieved between the data points and the linear fit in the investigated conditions. The expressions of K_1 and K_2 are:

$$K_1 = \exp\left(\frac{-5100}{T} + 1.62\right) \quad (24)$$

$$K_2 = \exp\left(\frac{-15299}{T} + 33.4\right) \quad (25)$$

Therefore, the dissociation flux in different stages can be expressed as:

$$F_1 = \exp\left(\frac{-5100}{T} + 1.62\right) RT \ln \frac{f_e}{f}, \text{ Stage 1}; \quad (26)$$

$$F_2 = \exp\left(\frac{-15299}{T} + 33.4\right) RT \ln \frac{C_e}{C}, \text{ Stage 2}. \quad (27)$$

3.2.4. Influence of capsule volume

Time evolutions of the gas regeneration profiles for the spherical capsule with different volumes are simulated and the results are shown in Fig. 13. As expected, t_{90} increases with the increase of capsule volume. Table 4 lists the values of n_{90} , t_{90} and average gas generation rate per volume for different capsule sizes. It can be noted that the average gas generation rate is higher for a larger capsule, due to a larger surface area. However, the average gas generation rate per volume decreases with the increasing capsule volume. The main reason is the higher surface-to-volume ratio for the smaller capsule size. Since the dissociation happens at the surface of gas hydrate, surface area will be the dominant factor in each stage of the dissociation process at a given temperature and pressure condition.

3.2.5. Influence of capsule geometry

Based on the results and discussions above, two major factors affect the dissociation kinetics of gas hydrate in a capsule: the dissociation driving force and dissociation surface area, and both factors are affected by the capsule geometry. To further investigate the effects of capsule geometry on gas hydrate dissociation kinetics, two other deformation structures of the RBC-shaped capsule, i.e., the ring-shaped and drum-shaped structures are designed with the same internal volume as that of the spherical and RBC-shaped capsules studied earlier. It can be considered that the radius of arc at the centre of RBC is zero for the ring shape and infinity for the drum shape. Table 5 shows the schematic and surface-to-volume ratio of the four geometries. The dissociation process of gas hydrate in the four capsules were simulated under 1 bar and 24 °C.

The values of t_{90} of each geometry are also shown in Table 5, and the amount of gas generation yield over time for different capsules are plotted in Fig. 14.

As can be observed, the semi-clathrate hydrate dissociation kinetics of the ring-shaped capsule is significantly enhanced compared to other shapes. This can be attributed to two reasons. Firstly, the surface-to-volume ratio of the ring-shaped capsule is the highest among the four geometries, which allows for the highest surface area for gas dissociation. Secondly, larger amount of hydrate dissociates in the rapid dissociation stage (Stage 1), leading to a shorter overall gas regeneration time. For the drum-shaped capsule, although the surface area is higher than the spherical one, its dissociation rate is lower since only a small amount of hydrate dissociates in the rapid dissociation stage, which results in a longer overall gas regeneration time.

In real applications, gas hydrate dissociation kinetics can be controlled by capsule geometry to meet actual demands. For instance, during gas hydrate transportation where low dissociation rate is desired to improve transport safety, RBC is overall the best as it allows high-efficiency hydrate formation while slow dissociation. In such cases, capsules with a lower surface-to-volume ratio and a shorter Stage 1 are more favourable. On the other hand, for gas regeneration devices where efficient dissociation is desired, capsules with higher surface-to-volume ratio and longer Stage 1 are more favourable, such as the ring shape.

4. Conclusions

In this paper, a new two-stage numerical model was proposed for the first time to investigate CO₂-TBAB semi-clathrate hydrate dissociation behaviour in individual capsules. The model was validated by experiments under various temperature and pressure conditions above the phase equilibrium curve of hydrate. The effects of temperature, pressure, capsule volume and capsule geometry on gas hydrate dissociation kinetics were investigated. The main findings conclude that:

- (1) Gas hydrate dissociation in a capsule can be divided into rapid dissociation stage (Stage 1) and slow dissociation stage (Stage 2). The variation in dissociation rate can be attributed to the change in dissociation surface area and the different mechanisms of driving force in the two stages. In both stages, the dissociation driving force can be expressed as the difference in Gibbs free energy between the hydrate phase under three-phase equilibrium condition and ambient phase. The reaction rate constants in both stages can be fitted into Arrhenius-type equations.

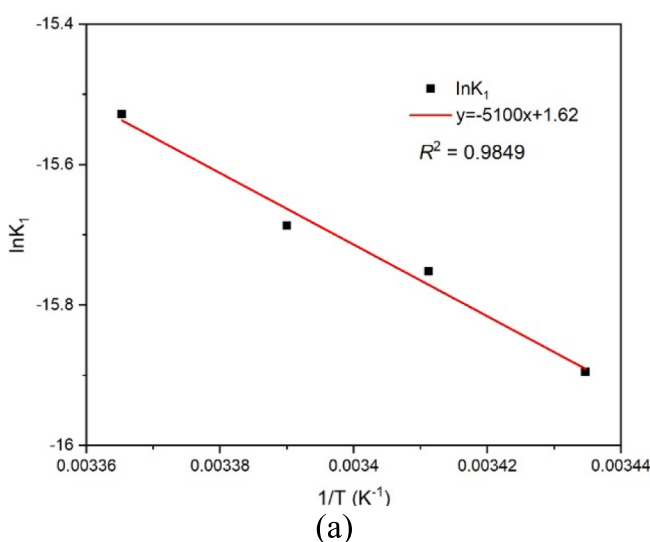
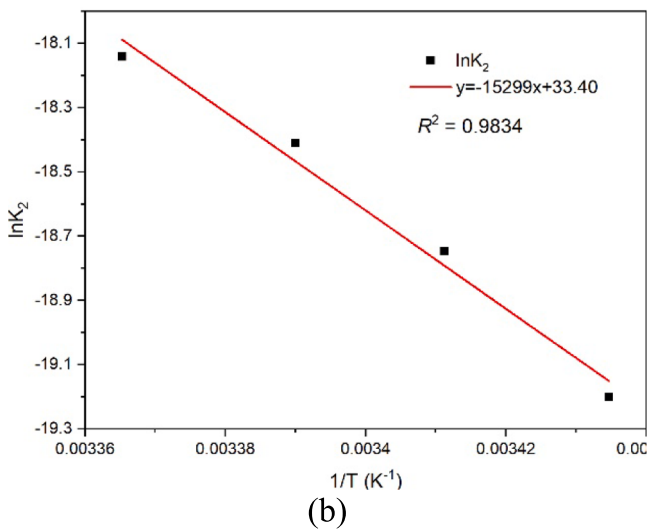


Fig. 12. Dependency of K_1 and K_2 on the temperature.



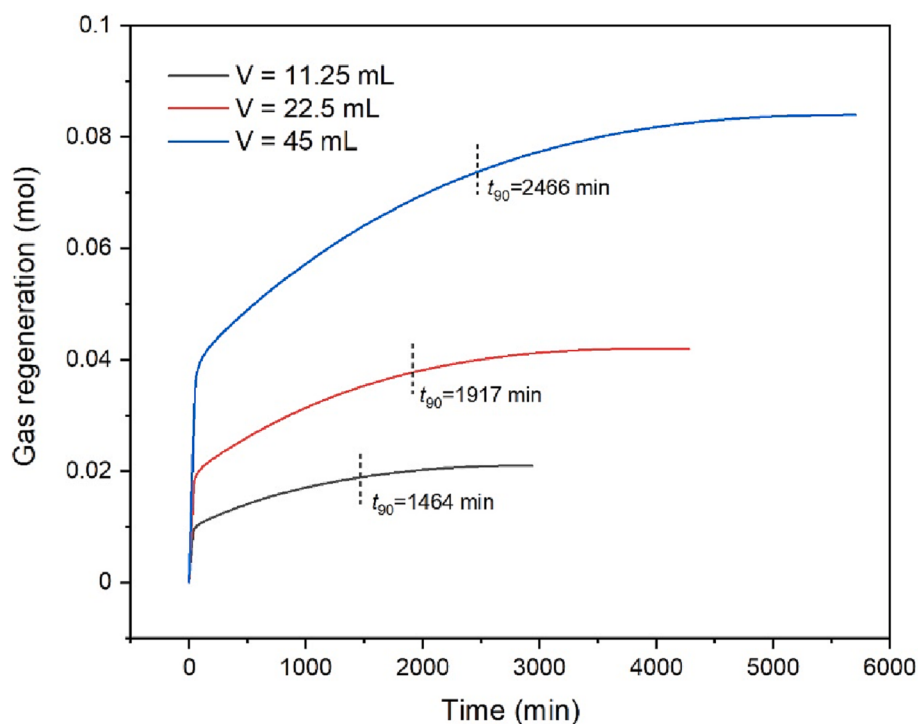


Fig. 13. Influence of capsule volume on gas regeneration.

Table 4
Influence of capsule volume on gas hydrate dissociation behaviour.

Capsule volume (mL)	n_{90} (mol)	t_{90} (min)	Average gas generation rate ($\times 10^5$ mol min $^{-1}$)	Average gas generation rate per volume (mol min $^{-1}$ m $^{-3}$)
11.25	0.01890	1,464	1.291	1.148
22.5	0.03780	1,917	1.972	0.8764
45	0.07560	2,466	3.066	0.6813

- (2) For encapsulated gas hydrate in a given shape, the average gas regeneration rate per volume decreases with the increasing capsule volume, due to the higher surface-to-volume ratio for the smaller capsule size.
- (3) Gas hydrate dissociation in a ring-shaped capsule has shortest overall dissociation time in the investigated capsule geometries

due to its high surface-to-volume ratio and long transition time to Stage 2.

This work provides an experimentally validated model for encapsulated gas hydrate and demonstrates the improvements of dissociation efficiency by tailoring the individual capsule shape. The numerical framework can be used for guiding the capsule design for relevant application scenarios. Future work can include the implementations of manipulation of dissociation for efficient hydrate-based gas transport and recovery.

Declaration of Competing Interest

The authors declare the following financial interests/personal relationships which may be considered as potential competing interests: Xiaolin Wang reports financial support was provided by Australian Research Council.

Table 5
Influence of capsule geometry on gas hydrate dissociation behaviour.

Shape	ring	RBC	drum	sphere
Schematic of the longitudinal section at transition point				
Surface-to-volume ratio (m $^{-1}$)	284	272	270	188
t_{90} (min)	718	2,215	2,495	1,917

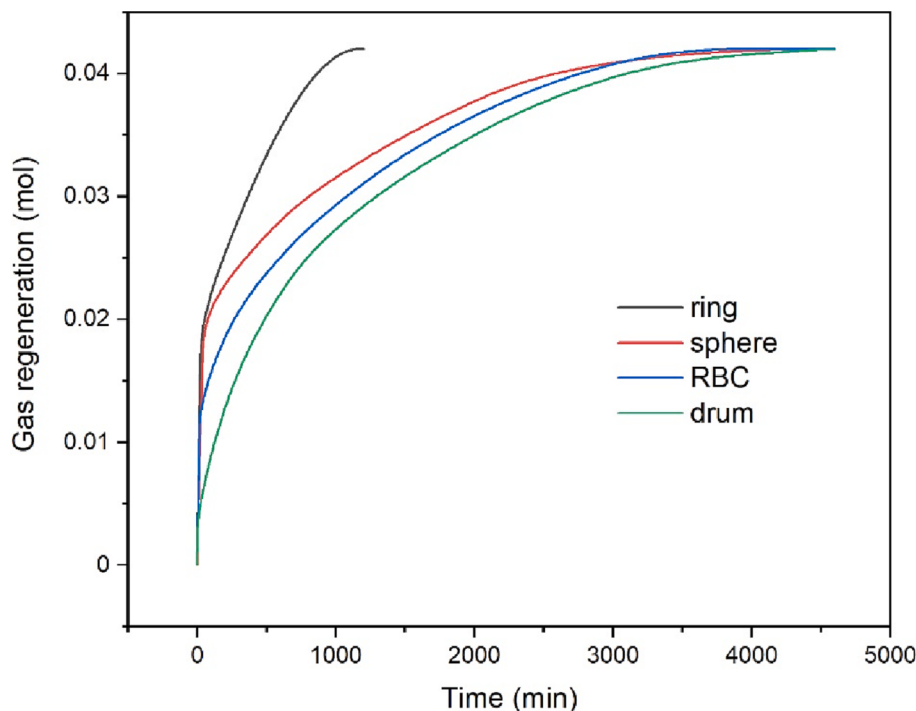


Fig. 14. Influence of capsule geometry on gas regeneration.

Data availability

Data will be made available on request.

Acknowledgements

This work was supported by Dr. Xiaolin Wang's Australian Research Council Discovery Early Career Researcher Award (Project number: DE200100326) funded by the Australian Government. Dr. Benjapon Chalermsinsuwan is the recipient of Thailand Science Research and Innovation Fund Chulalongkorn University, Thailand (DIS66230001).

References

- [1] K.Z. House, D.P. Schrag, C.F. Harvey, K.S. Lackner, Permanent carbon dioxide storage in deep-sea sediments, *PNAS* 103 (33) (2006) 12291–12295.
- [2] D. Lee, Y. Lee, J. Lim, Y. Seo, Guest enclathration and structural transition in CO₂+N₂+methylcyclopentane hydrates and their significance for CO₂ capture and sequestration, *Chem. Eng. J.* 320 (2017) 43–49.
- [3] Z. Xia, X. Li, Z. Chen, G. Li, Y.i. Wang, C. Jing, Z. Li, Q. Lv, Hydrate-based synchronously capture of CO₂ and H₂S for clean H₂ with new synergic additives, *Energy Procedia* 142 (2017) 3427–3432.
- [4] B. Prah, R. Yun, CO₂ hydrate slurry transportation in carbon capture and storage, *Appl. Therm. Eng.* 128 (2018) 653–661.
- [5] A. Azimi, M. Mirzaei, Experimental evaluation and thermodynamic modeling of hydrate selectivity in separation of CO₂ and CH₄, *Chem. Eng. Res. Des.* 111 (2016) 262–268.
- [6] L. Fournaison, A. Delahaye, I. Chatti, J.-P. Petitet, CO₂ hydrates in refrigeration processes, *Ind. Eng. Chem. Res.* 43 (20) (2004) 6521–6526.
- [7] P. Babu, C.Y. Ho, R. Kumar, P. Linga, Enhanced kinetics for the clathrate process in a fixed bed reactor in the presence of liquid promoters for pre-combustion carbon dioxide capture, *Energy* 70 (2014) 664–673.
- [8] S. Nakano, K.-H. Chang, A. Shijima, H. Miyamoto, Y. Sato, Y. Noto, J.-Y. Ha, M. Sakamoto, A usage of CO₂ hydrate: Convenient method to increase CO₂ concentration in culturing algae, *Bioresour. Technol.* 172 (2014) 444–448.
- [9] J. Lee, S. Park, W. Sung, An experimental study on the productivity of dissociated gas from gas hydrate by depressurization scheme, *Energ. Conver. Manage.* 51 (12) (2010) 2510–2515.
- [10] H. Liang, Y. Song, Y. Chen, Numerical simulation for laboratory-scale methane hydrate dissociation by depressurization, *Energ. Conver. Manage.* 51 (10) (2010) 1883–1890.
- [11] T. Collett, J.-J. Bahk, R. Baker, R. Boswell, D. Divins, M. Frye, D. Goldberg, J. Husebø, C. Koh, M. Malone, M. Morell, G. Myers, C. Shipp, M. Torres, Methane hydrates in nature current knowledge and challenges, *J. Chem. Eng. Data* 60 (2) (2015) 319–329.
- [12] X. Kou, et al., Distribution and reformation characteristics of gas hydrate during hydrate dissociation by thermal stimulation and depressurization methods, *Appl. Energy* 277 (2020), 115575.
- [13] M. Aminnajafi, B. Tohidi, R. Burgass, M. Atilhan, Gas hydrate blockage removal using chemical injection in vertical pipes, *J. Nat. Gas Sci. Eng.* 40 (2017) 17–23.
- [14] Z. Yin, G. Moridis, Z.R. Chong, H.K. Tan, P. Linga, Numerical analysis of experimental studies of methane hydrate dissociation induced by depressurization in a sandy porous medium, *Appl. Energy* 230 (2018) 444–459.
- [15] X. Yang, C.-Y. Sun, K.-H. Su, Q. Yuan, Q.-P. Li, G.-J. Chen, A three-dimensional study on the formation and dissociation of methane hydrate in porous sediment by depressurization, *Energ. Conver. Manage.* 56 (2012) 1–7.
- [16] L. Zhan, Y. Wang, X.-S. Li, Experimental study on characteristics of methane hydrate formation and dissociation in porous medium with different particle sizes using depressurization, *Fuel* 230 (2018) 37–44.
- [17] L. Xiong, X. Li, Y.i. Wang, C. Xu, Experimental study on methane hydrate dissociation by depressurization in porous sediments, *Energies* 5 (2) (2012) 518–530.
- [18] G.D. Holder, P.F. Angert, V.T. John, S. Yen, A thermodynamic evaluation of thermal recovery of gas from hydrates in the earth (includes associated papers 11863 and 11924), *J. Petrol. Tech.* 34 (05) (1982) 1127–1132.
- [19] Z. Yin, Z.R. Chong, H.K. Tan, P. Linga, Review of gas hydrate dissociation kinetic models for energy recovery, *J. Nat. Gas Sci. Eng.* 35 (2016) 1362–1387.
- [20] H.C. Kim, P.R. Bishnoi, R.A. Heidemann, S.S.H. Rizvi, Kinetics of methane hydrate decomposition, *Chem. Eng. Sci.* 42 (7) (1987) 1645–1653.
- [21] M.A. Clarke, P. Bishnoi, Determination of the intrinsic kinetics of CO₂ gas hydrate formation using in situ particle size analysis, *Chem. Eng. Sci.* 60 (3) (2005) 695–709.
- [22] H. Hong, M. Pooladi-Darvish, Simulation of depressurization for gas production from gas hydrate reservoirs, *J. Can. Pet. Technol.* 44 (11) (2005).
- [23] X. Cao, K. Yang, J. Bian, Investigation of CO₂ hydrate slurry flow characteristics with particle dissociation for carbon storage and transportation, *Process Saf. Environ. Prot.* 152 (2021) 427–440.
- [24] L. Dong, Y. Li, N. Wu, Y. Wan, H. Liao, H. Wang, Y. Zhang, Y. Ji, G. Hu, Y. Leonenko, Numerical simulation of gas extraction performance from hydrate reservoirs using double-well systems, *Energy* 265 (2023), 126382.
- [25] P. Wu, et al., Microstructure evolution and dynamic permeability anisotropy during hydrate dissociation in sediment under stress state, *Energy* 263 (2023), 126126.
- [26] M.A. Clarke, P. Bishnoi, Determination of the intrinsic rate constant and activation energy of CO₂ gas hydrate decomposition using in-situ particle size analysis, *Chem. Eng. Sci.* 59 (14) (2004) 2983–2993.
- [27] Y. Jiang, et al., Numerical simulation on the evolution of physical and mechanical characteristics of natural gas hydrate reservoir during depressurization production, *J. Nat. Gas Sci. Eng.* 108 (2022), 104803.
- [28] Y. Hao, S. Yang, Y. Guo, F. Yang, S. Li, C. Wang, X. Xiao, The effects of time variable fracture conductivity on gas production of horizontal well fracturing in natural gas hydrate reservoirs, *Energy Sci. Eng.* 10 (12) (2022) 4840–4858.

- [29] D. Wu, et al., A novel model of reaction specific surface area via depressurization and thermal stimulation integrating hydrate pore morphology evolution in porous media, *Chem. Eng. J.* 452 (2023), 139097.
- [30] X. Sun, K.K. Mohanty, Kinetic simulation of methane hydrate formation and dissociation in porous media, *Chem. Eng. Sci.* 61 (11) (2006) 3476–3495.
- [31] W.-Y. Sean, T. Sato, A. Yamasaki, F. Kiyono, CFD and experimental study on methane hydrate dissociation Part I, *Dissociation under water flow*. *AIChE journal* 53 (1) (2007) 262–274.
- [32] W.-Y. Sean, T. Sato, A. Yamasaki, F. Kiyono, CFD and experimental study on methane hydrate dissociation, *Part II. General cases*. *AIChE journal* 53 (8) (2007) 2148–2160.
- [33] S.-M. Jeong, L.-H. Chiang Hsieh, C.-Y. Huang, W.-Y. Sean, Direct numerical simulation of CO₂ hydrate dissociation in pore-scale flow by applying CFD method, *Int. J. Heat Mass Transf.* 107 (2017) 300–306.
- [34] A. Fukumoto, W.-Y. Sean, T. Sato, A. Yamasaki, F. Kiyono, Estimation of dissociation rate constant of CO₂ hydrate in water flow, *Greenhouse Gases Sci. Technol.* 5 (2) (2015) 169–179.
- [35] R. Song, et al., Pore scale modeling on dissociation and transportation of methane hydrate in porous sediments, *Energy* 237 (2021), 121630.
- [36] X. Ruan, Y. Song, H. Liang, M. Yang, B. Dou, Numerical simulation of the gas production behavior of hydrate dissociation by depressurization in hydrate-bearing porous medium, *Energy Fuel* 26 (3) (2012) 1681–1694.
- [37] X. Cao, et al., Numerical simulation of hydrate particle behaviors in gas-liquid flow for horizontal and inclined pipeline, *Case Studies Thermal Eng.* 27 (2021), 101294.
- [38] X. Cao, et al., Modelling of hydrate dissociation in multiphase flow considering particle behaviors, mass and heat transfer, *Fuel* 306 (2021), 121655.
- [39] Y. Zhang, X. Zhai, F. Zhang, Z. Zhang, K. Hooman, H. Zhang, X. Wang, A biomimetic red blood cell inspired encapsulation design for advanced hydrate-based carbon capture, *Energy* 271 (2023), 126985.
- [40] X. Wang, M. Dennis, Phase equilibrium and formation behaviour of CO₂-TBAB semi-clathrate hydrate at low pressures for cold storage air conditioning applications, *Chem. Eng. Sci.* 155 (2016) 294–305.
- [41] P. Paricaud, Modeling the dissociation conditions of salt hydrates and gas semiclathrate hydrates: application to lithium bromide, hydrogen iodide, and tetrabutylammonium bromide+ carbon dioxide systems, *J. Phys. Chem. B* 115 (2) (2011) 288–299.
- [42] L.W. Diamond, N.N. Akinfiev, Solubility of CO₂ in water from – 1.5 to 100 C and from 0.1 to 100 MPa: evaluation of literature data and thermodynamic modelling, *Fluid Phase Equilib.* 208 (1–2) (2003) 265–290.
- [43] R.F. Weiss, Carbon dioxide in water and seawater: the solubility of a non-ideal gas, *Mar. Chem.* 2 (3) (1974) 203–215.
- [44] Z. Li, L. Yuan, G. Sun, J. Lv, Y.i. Zhang, Experimental determination of CO₂ diffusion coefficient in a brine-saturated core simulating reservoir condition, *Energies* 14 (3) (2021) 540.
- [45] H. Hashemi, S. Babaei, A.H. Mohammadi, P. Naidoo, D. Ramjugernath, State of the art and kinetics of refrigerant hydrate formation, *Int. J. Refrig.* 98 (2019) 410–427.
- [46] A. Ranganathan, The levenberg-marquardt algorithm, *Tutorial LM Algorithm* 11 (1) (2004) 101–110.
- [47] F. Zhang, X. Wang, B.o. Wang, X. Lou, W. Lipiński, Experimental and numerical analysis of CO₂ and CH₄ hydrate formation kinetics in microparticles: A comparative study based on shrinking core model, *Chem. Eng. J.* 446 (2022), 137247.